CO_2 Reduction Hot Paper

How to cite: *Angew. Chem. Int. Ed.* **2023,** *62,* e202217220
International Edition: doi.org/10.1002/anie.202217220
German Edition: doi.org/10.1002/ange.202217220

Electronic Perturbation of Copper Single-Atom CO_2 Reduction Catalysts in a Molecular Way

Haiyuan Zou[+], Gang Zhao[+], Hao Dai, Hongliang Dong, Wen Luo, Lei Wang, Zhouguang Lu, Yi Luo, Guozhen Zhang, and Lele Duan**

Abstract: Fine-tuning electronic structures of single-atom catalysts (SACs) plays a crucial role in harnessing their catalytic activities, yet challenges remain at a molecular scale in a controlled fashion. By tailoring the structure of graphdiyne (GDY) with electron-withdrawing/-donating groups, we show herein the electronic perturbation of Cu single-atom CO_2 reduction catalysts in a molecular way. The elaborately introduced functional groups (–F, –H and –OMe) can regulate the valance state of $Cu^{\delta+}$, which is found to be directly scaled with the selectivity of the electrochemical CO_2-to-CH_4 conversion. An optimum CH_4 Faradaic efficiency of 72.3 % was achieved over the Cu SAC on the F-substituted GDY. In situ spectroscopic studies and theoretical calculations revealed that the positive $Cu^{\delta+}$ centers adjusted by the electron-withdrawing group decrease the pK_a of adsorbed H_2O, promoting the hydrogenation of intermediates toward the CH_4 production. Our strategy paves the way for precise electronic perturbation of SACs toward efficient electrocatalysis.

Introduction

Electronic perturbations of the catalytic site play a vital role in improving the activity and selectivity of catalysts across the fields of energy conversion, chemical transformation and environmental remediation.[1] For example, surface $Cu^{\delta+}$ species of copper catalysts in the electrochemical CO_2 reduction reaction (CO_2RR) preferentially show multi-electron reduction processes compared to Cu^0, leading to the formation of deeply reduced carbon products.[2] Great efforts have thus aimed at steering the CO_2RR reactivity via the electronic regulation of catalytic centers.[3] Prevalently, exquisite electronic regulation of the catalytic site at the atomic level has long been utilized for optimizing homogeneous catalysts by introducing specific ligands/functional groups around the metal centers.[4] As such, leveraging the molecular strategy to regulate the electronic structure of heterogeneous centers may enable the deterministic design of more selective and active heterogeneous catalysts. Of particular interest, electronic perturbation of single-atom catalysts (SACs) at molecular precision would foster the optimal catalytic activity and deepen the structure-function relationships, which, however, still remains a critical challenge.[5]

Among the prevalent SACs on carbon materials explored to date, regulation of the electronic structure of active centers hinges on the strategies such as pyrolyzing, doping and defecting, which have offered limited versatility to tune the electronic structures of the metal centers at the molecular level.[6] The difficulty arises from the lack of control in precisely tailoring the surrounding coordination environments of the active center, which the nature of the electronic structure relied on. As a new carbon allotrope, graphdiyne (GDY), forms SACs with various transition metals via the coordination between the metal atom and the C≡C triple bond.[7] Tens of GDY derivatives have been prepared by deliberately installing functional groups with various electron-donating and -withdrawing capabilities.[8] Therefore, the precise functionalization of GDY affords a molecular toolkit for flexible and accurate perturbation of the electronic structures of GDY-based SACs, which would

[*] Dr. H. Zou,[+] H. Dai, Prof. L. Duan
Department of Chemistry and Shenzhen Grubbs Institute, Southern University of Science and Technology
Shenzhen 518055 (P. R. China)
E-mail: duanll@sustech.edu.cn

G. Zhao,[+] Prof. Y. Luo, Dr. G. Zhang
Hefei National Laboratory for Physical Sciences at the Microscale, University of Science and Technology of China
Hefei 230026 (China)
E-mail: guozhen@ustc.edu.cn

Dr. H. Dong
Center for High Pressure Science and Technology Advanced Research
Pudong, Shanghai 201203 (China)

W. Luo, Prof. Z. Lu
Department of Materials Science and Engineering, Southern University of Science and Technology
Shenzhen 518055 (China)

Prof. L. Wang
Department of Chemical and Biomolecular Engineering, National University of Singapore
Singapore 117585 (Singapore)

[+] These authors contributed equally to this work.

extend the boundaries of homogeneous and heterogeneous catalysts.

With the view to systematically regulating the electronic structures of SACs, we tailored the GDY support by introducing electron-withdrawing and -donating groups (–F, –H and –OMe) to synthesize GDY derivatives R-GDY (R = –F, –H or –OMe), and realized densely populated Cu SACs (denoted as Cu SA/R-GDY; Figure 1a) through a facile bottom-up synthetic strategy. Taking advantage of the unique structures of R-GDY, the Cu atoms can be confined to form atomic Cu–C_4 moiety, while their electronic structures are precisely perturbated by the neighboring functional groups, rendering the $Cu^{\delta+}$ valance state in the order of Cu SA/F-GDY > Cu SA/H-GDY > Cu SA/OMe-GDY. We further leveraged the CO_2RR for proof-of-principle applications. Our results revealed that the selectivity of CH_4 on Cu SA/R-GDY was proportional to the electron-withdrawing ability of surrounding functional groups. The optimum CH_4 Faradaic efficiency (FE_{CH_4}) of 72.3 % was achieved by Cu SA/F-GDY at −1.2 V versus a reversible hydrogen electrode (RHE), accompanied by a partial current density (j_{CH_4}) of −174.24 mA cm^{-2}. In situ spectroscopic studies of surface-enhanced Raman spectroscopy, electron energy loss spectroscopy (EELS) and attenuated total reflection Fourier-transform infrared spectroscopy (ATR-FTIR) together with theoretical insights suggested that the preferred CH_4 formation originated from the positively charged $Cu^{\delta+}$ induced by the electron-withdrawing –F group, which lowers the pK_a of adsorbed H_2O and provides a microenvironment at suitable pH for CH_4 production.

Results and Discussion

Firstly, *para*-di-substituted 1,2,4,5-tetraethynylbenzene monomers with distinctive electron-donating/-withdrawing groups of –OMe, –H and –F were synthesized according to the documented procedures (see the Supporting Information for details, Scheme S1 for the synthetic scheme, and Figure S1–S3 for nuclear magnetic resonance spectra (NMR) of compounds). Next, Cu SA/R-GDY was prepared by a facile

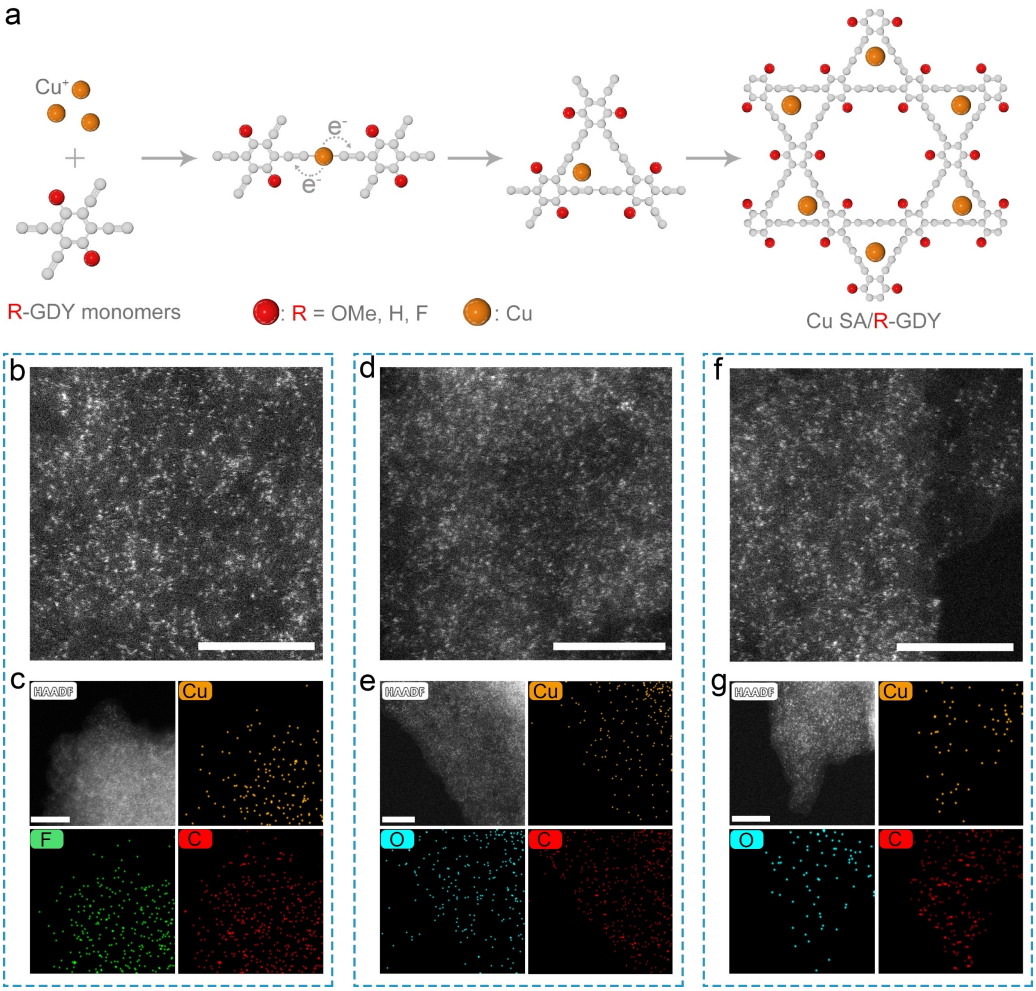

Figure 1. Morphologies of Cu SA/R-GDY. a) Schematic illustration of the fabrication of Cu SA/R-GDY (R = –F, –H, –OMe). HAADF-STEM images of b) Cu SA/F-GDY, d) Cu SA/H-GDY and f) Cu SA/OMe-GDY. EDX mapping of c) Cu SA/F-GDY, e) Cu SA/H-GDY and g) Cu SA/OMe-GDY. Scale bar is 5 nm.

bottom-up synthetic approach using the corresponding *para*-di-substituted 1,2,4,5-tetraethynylbenzene monomers. Briefly, an appropriate amount of CuI was mixed with *para*-di-substituted 1,2,4,5-tetraethynylbenzene monomers in pyridine, and the solution then sequentially underwent reductive elimination and cross-coupling processes, leading to the formation of R-GDY and confined Cu single atoms on the R-GDY derivatives via Cu–C interactions (Figure 1a). The obtained samples were fully characterized by Raman, FTIR spectroscopy and X-ray photoelectron spectroscopy (XPS).

As shown in Figure S4a, the synthesized samples render analogous Raman profiles with a clear D-band (disordered carbon, 1356 cm^{-1}) and G-band (graphite carbon, 1576 cm^{-1}); other peaks at 2180 and 2250 cm^{-1} are aroused by the diacetylene linkages vibrations, signifying the GDY-like feature. For the FTIR spectra (Figure S4b), the stretching vibration bands of C–F (900 cm^{-1}) or C–OMe (1200 cm^{-1}) are exclusively observed in Cu SA/F-GDY and Cu SA/OMe-GDY, respectively. In the XPS spectra, the high-resolution C 1s spectra show characteristic C=C (sp2) and C≡C (sp) peaks in the prepared samples. Besides, the C–F bond at 286.6 eV and C–OMe bond at 286.2 eV are observed for Cu SA/F-GDY and Cu SA/OMe-GDY, respectively (Figure S5). The combined results revealed that functional groups-modified R-GDY materials were successfully synthesized.

The atomically dispersed Cu atoms were imaged by aberration-corrected high-angle annular dark-field scanning transmission electron microscopy (HAADF-STEM), where dense but isolated bright dots are clearly observed in various regions (Figure 1b, d, f and Figure S6). As such, high Cu loadings of 12.8 wt %, 12.3 wt % and 13.4 wt % estimated by the inductively coupled plasma atomic emission spectroscopy (ICP-AES) were achieved for Cu SA/F-GDY, Cu SA/H-GDY and Cu SA/OMe-GDY, respectively. In addition, the atomic-scale energy-dispersive X-ray spectroscopy (EDX) presented homogeneously distributed elements of C, Cu, O (in Cu SA/OMe-GDY and Cu SA/H-GDY) and C, Cu, F (in Cu SA/F-GDY) cross the entire regions (Figures 1c, e and g). Low magnification TEM characterizations of Cu SA/R-GDY indicate a lateral size with no nanoparticle visualized (Figures S7–S9). The X-ray diffraction (XRD) patterns also reflected the absence of crystalline Cu nanoparticles, where only a broad peak of carbon substrate is observed (Figure S10).

The electronic and local coordination structures of Cu SA/R-GDY were identified by X-ray absorption fine structure (XAFS) analysis. Our results showcase that the charge states of Cu centers of Cu SA/R-GDY could be perturbed in atomic precision by the surrounding functional groups. Figure 2a presents the X-ray absorption near-edge spectra (XANES) of Cu *K*-edge for Cu foil, CuI and the prepared samples. The near-edge position and the corresponding derivative of Cu *K*-edge XANES of Cu SA/R-GDY lie between those of Cu foil and CuI, confirming the $Cu^{\delta+}$ $(0<\delta<1)$ state of the Cu centers (Figures 2a and S11). Of note, both the near-edge position and their derivative

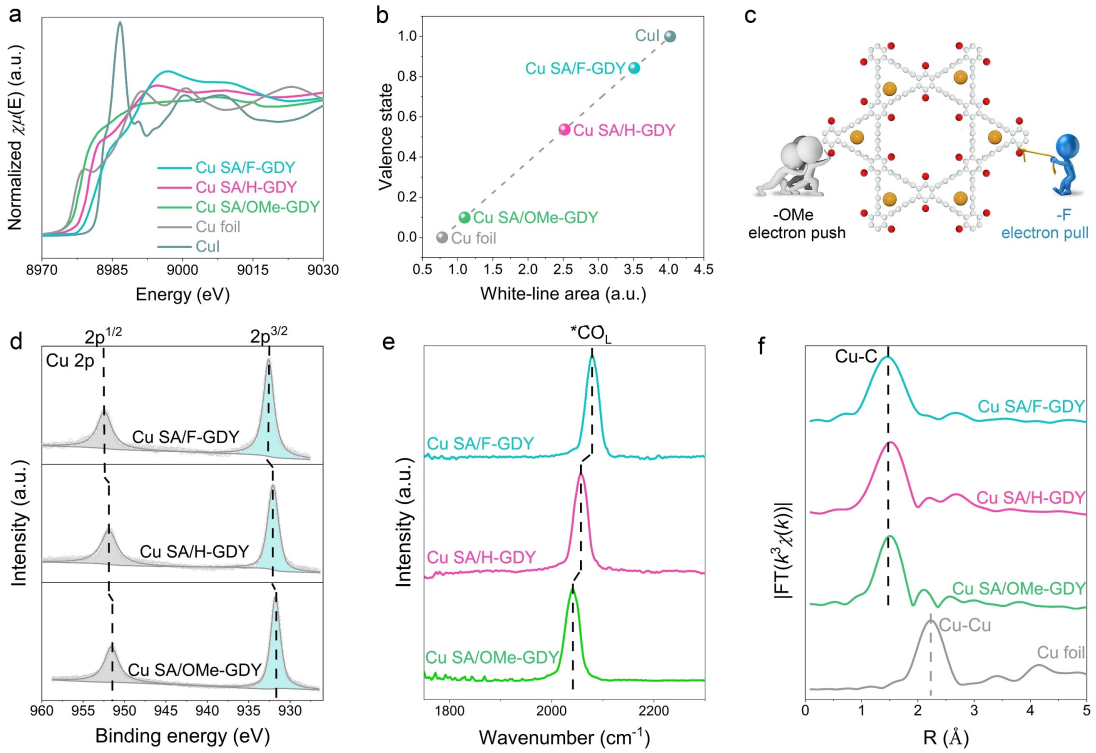

Figure 2. Cu SA/R-GDY structural analysis. a) XANES spectra and b) the average valance state of the prepared Cu SA/R-GDY with reference Cu foil and CuI. c) Schematic illustration of electron-push-pull. d) XPS spectra of Cu 2*p*. e) CO-probed DRIFT spectra. f) Cu k^3-weighted FT-EXAFS spectra in R space.

shift positively by varying the functional groups from electron-donating to electron-withdrawing ones. Moreover, the white-line intensity of Cu *K*-edge grows as the electron-withdrawing ability of the functional group increases. The charge state of Cu estimated by the integrated area of white-line intensity is calculated to be +0.86 for Cu SA/F-GDY, higher than those of Cu SA/H-GDY (+0.56) and Cu SA/OMe-GDY (+0.23) (Figure 2b). The core-level XPS spectra of Cu 2*p* in Figure 2d further corroborate the electronic perturbation of $Cu^{\delta+}$, wherein the spin-orbit peaks of Cu $2p^{3/2}$ and Cu $2p^{1/2}$ are consistently shifted to the lower energy direction from Cu SA/F-GDY, to Cu SA/H-GDY and further to Cu SA/OMe-GDY.[9] The additional Auger electron spectroscopy (AES) of Cu LMM also reveals that Cu SA/F-GDY displays the highest valence state of Cu, followed by Cu SA/H-GDY and then Cu SA/OMe-GDY (Figure S12). *All the above results demonstrated that fine-tuning the electronic structure of Cu single-atom catalysts was realized by tailoring the surrounding functional groups in a molecular way (Figure 2c), just like the structural optimization for homogeneous catalysts.*

The diffuse reflectance infrared Fourier transform (DRIFT) spectra of Cu SA/R-GDY upon CO adsorption manifests a prominent linearly bonded CO (CO_L) band at $\approx$2050 cm^{-1},[10] implying that the CO molecules are adsorbed on Cu single-atoms (Figure 2e). Moreover, the absence of bridge bonded CO band in the range of 1700–1900 cm^{-1} ruled out the presence of multi-atom Cu resembles in Cu SA/R-GDY. Notably, the CO_L peak shifted to the lower frequency direction from Cu SA/F-GDY to Cu SA/OMe-GDY, which is ascribed to the reduced oxidation state of Cu. Furthermore, the Fourier transformed k^2-weighted extended X-Ray absorption fine structure (EXAFS) and wavelet transformation (WT) EXAFS oscillations of Cu *K*-edge presented a dominant Cu–C peak at approximately 1.5 Å among Cu SA/R-GDY (Figures 2e and S13). In addition, no other typical bonds for Cu–Cu contribution at 2.2 Å were detected, indicating the atomic dispersion of Cu atoms in the materials. Meanwhile, the peaks of F 1s and O 1s XPS spectra of Cu SA/F-GDY and Cu SA/OMe are respectively attributed to C–F and –OMe (with minor surface adsorbed water) groups, indicating that the introduced functional groups do not coordinate with Cu (Figure S14).[11] The EXAFS fitting results demonstrated that the first shell of the atomic Cu center renders a coordination number close to 4, resembling the Cu coordination structure to Cu–C_4 moieties confined by the alkyne bond on R-GDY frameworks (Figure S15 and Table S2). Thus, the electron-donating/-withdrawing groups feature a "charge-state-modulator" to precisely regulate the electron density of Cu–C_4 centers.

The abundant Cu–C_4 active centers with fine-tuned electronic structures render as-developed materials excellent candidates for electrochemical catalysis and models for studying the structure-function relationship. As a proof-of-principle demonstration, we leveraged the CO_2RR to elucidate the structure–activity relationship (electronic structure or Cu charge state versus product selectivity).

In general, CO_2RR activity was evaluated in a microfluidic flow cell reactor with 1.0 M KOH as the electrolyte (Figure S16), and the output gaseous and liquid-phase products were quantified by the gas chromatography (GC) and NMR spectroscopy, respectively. All the potentials are converted to RHE unless otherwise specified. Linear sweep voltammetry (LSV) was first assessed in CO_2- and Ar-purged conditions for Cu SA/R-GDY. As shown in Figure S17, Cu SA/F-GDY afforded a more positive onset potential and a higher current density than the other two samples, signifying its fast CO_2RR response. Such favorable CO_2RR kinetics on Cu SA/F-GDY was also reflected by a larger current density gap in CO_2- over Ar-purged LSV curves. Then, the CO_2RR product distributions and the FE as the function of applied potentials from −0.7 V to −1.3 V were deployed to study the catalytic behavior over the Cu SA/R-GDY. For Cu SA/OMe-GDY, the by-product of H_2 is overwhelmed to the CO_2RR product of CO, CH_4, HCOOH and C_2H_4, crossing the potential windows (Figure 3c). The total CO_2RR product reaches a maximum FE of 34.7 % at −1.3 V, and CO is favored over CH_4 and C_2H_4. Cu SA/H-GDY presented decreased H_2 selectivity compared with Cu SA/OMe-GDY, yet, the overall CO_2RR performance is moderate. As the potential shifted negatively, the FE_{CH4} increased stepwise at the expense of CO, and reached its optima of 51.3 % at −1.3 V (Figure 3b and Figure S18). In sharp contrast, when using Cu SA/F-GDY as an electrode, H_2 selectivity is significantly suppressed, while CH_4 selectivity is drastically boosted compared with the former two catalysts (Figure 3a and Figure S19a). The major CO_2RR product of CH_4 was produced preferentially at each exert potential with an optimum FE_{CH_4} of 72.3 % at −1.2 V, about 1.6 and 6.4 folds as much as those of Cu SA/H-GDY and Cu SA/OMe-GDY, respectively (Figure 3d). Meanwhile, the j_{CH_4} of Cu SA/F-GDY is much higher than its counterparts, yielding a maximum j_{CH_4} of 174.24 mA cm^{-2} (Figure S19b). Representative GC and NMR results of the Cu SA/F-GDY electrode operated at −1.2 V are shown in Figure S20. In addition, by extracting the FE for the two-electron products (FE_{C2e-}, e.g., CO, HCOOH) versus more than two-electron reaction cascade ($FE_{C>2e-}$, e.g., CH_4, C_2H_4), we found that Cu SA/F-GDY drives a $FE_{C>2e-}/FE_{C2e-}$ ratio of 9.33 at −1.2 V, which is 3.37 and 10.90 folds as high as those of Cu SA/H-GDY and Cu SA/OMe-GDY, respectively (Figure 3e and Figure S21). Such a high activity derived from Cu SA/F-GDY is on par with that of the top-of-the-class CO_2RR catalysts for CH_4 production.[12] Furthermore, the isotopic-labeling experiment was conducted using $^{13}CO_2$ as a feeding gas to verify the concrete carbon source of the products. As evidenced by the GC-MS spectra (Figure S22), the main signals at $m/z=17$, $m/z=29$ and $m/z=30$ belong to $^{13}CH_4$, ^{13}CO and $^{13}C_2H_4$, respectively, confirming that the origin of gas products derived from CO_2RR.

The contact angle values of Cu SA/R-GDY were all around 133°, revealing their highly hydrophobic nature (Figure S23). Thus, the surface hydrophobicity of the catalysts shall not significantly contribute to the variation of the CH_4 production rates. Furthermore, we estimated the turnover frequency (TOF) and mass activity over the as-

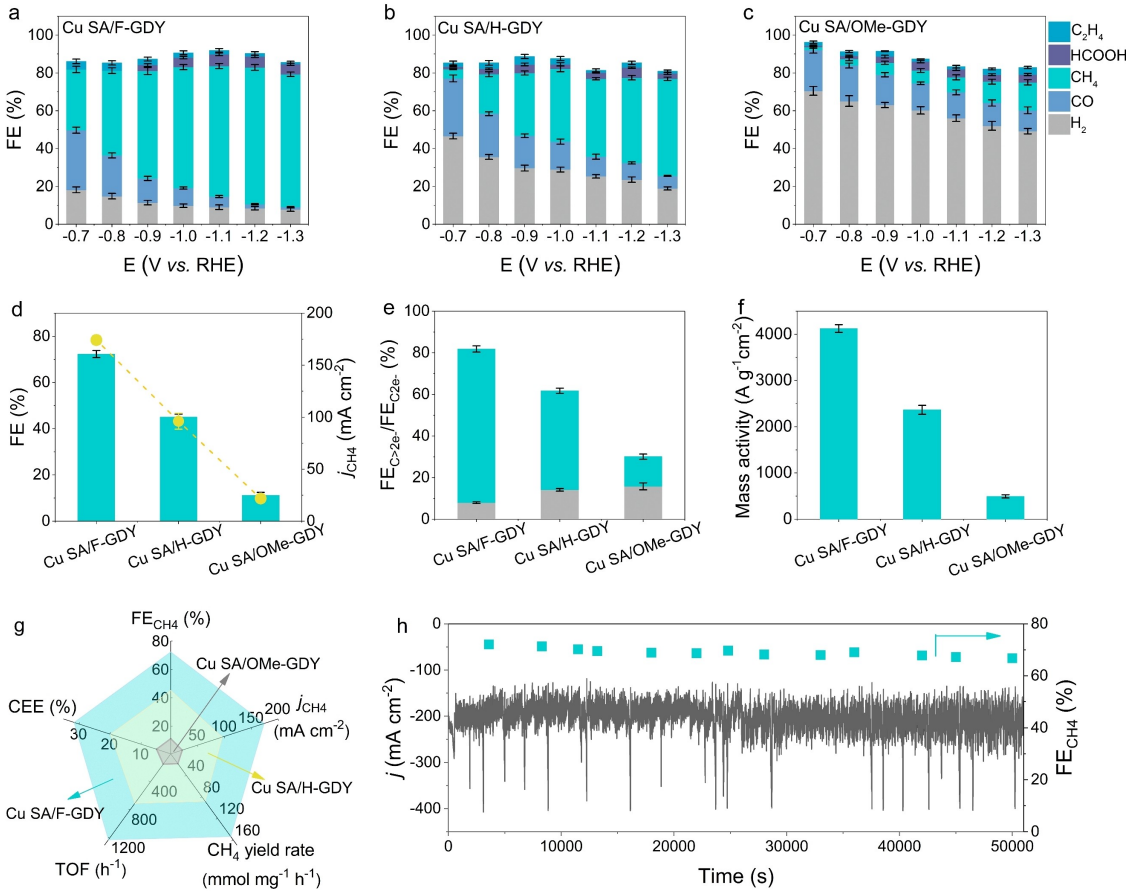

Figure 3. Electrochemical CO_2RR performance. FE for all products on a) Cu SA/F-GDY, b) Cu SA/H-GDY and c) Cu SA/OMe-GDY in 1 M KOH electrolyte. d) FE_{CH_4} and j_{CH_4} of Cu SA/R-GDY at −1.2 V. e) $FE_{C>2e-}/FE_{C2e-}$ ratios of Cu SA/R-GDY at −1.2 V. f) Mass activity of Cu SA/R-GDY at −1.2 V. g) Comparison of FE_{CH_4}, j_{CH_4}, CEE, TOF and CH_4 yield rate for Cu SA/R-GDY at −1.2 V. h) Stability test of Cu SA/F-GDY at −1.2 V.

obtained Cu single sites for the CH_4 production. Again, Cu SA/F-GDY exhibits considerably larger TOF and mass activity than the other two samples at each given potential (Figures S24 and S25). Especially, approximately an order of magnitude of TOF (1222.5 h^{-1}) and mass activity (4125 $A\,g^{-1}\,cm^{-2}$) was consistently improved by Cu SA/F-GDY than those of Cu SA/OMe-GDY (146.8 h^{-1} and 495.5 $A\,g^{-1}\,cm^{-2}$) at −1.2 V (Figure 3f). Consequently, a high CH_4 yield rate of 153.9 $mol\,mg_{Cu}^{-1}\,h^{-1}$ is achieved by Cu SA/F-GDY at −1.2 V (Figure S26). We also evaluated the half-cell energy conversion efficiency (CEE) for CH_4, which represents the proportion of chemical energy stored in the CH_4 product to the electrical energy required for the reaction. The maximum CEE for Cu SA/F-GDY was 31.54 %, suggesting that a significant part of electrical energy is accounted for the CH_4 formation (Figure S27). Figure 3g summarized and compared the major performance parameters of FE_{CH_4}, j_{CH_4}, TOF_{CH_4}, CH_4 yield rate and CEE against the applied potential of −1.2 V for Cu SA/R-GDY. Interestingly, the CO_2RR activity in terms of the presented key performance parameters is scaled directly with the electron-withdrawing ability of the introduced groups surrounding the active sites. Thus, we can conclude that the CO_2RR activity of Cu SA/R-GDY is steered by the distinct electronic structures of Cu atoms regulated by the surrounding electron-withdrawing/-donating groups.

Long-term electrolysis was carried out at a stationary potential of −1.2 V for 11 h to monitor the durability of Cu SA/F-GDY. As shown in Figure 3h, the overall current density shows no apparent decrease over the electrolysis course. Of note, the sudden current fluctuation may occur due to (i) the pressure change caused by the automatic sampling of GC and (ii) the burst of bubbles on the cathodic electrode. The slight decrease of FE_{CH_4} from 72.1 % to 65.3 % is ascribed to flooding. Careful XRD, XPS, Raman and HADDF-STEM characterizations of the post-tested Cu SA/F-GDY elucidated well-maintained atomic and densely-populated Cu structure (Figures S28 and S29).

To gain molecular-level insight into the role of the functional groups, we conducted in situ surface-enhanced Raman spectroscopy (SERS) in a spectro-electrochemical flow cell (Figure S30). Since the Cu single atoms possess no SERS phenomenon, shell-isolated nanoparticle-enhanced Raman spectroscopy (SHINERS) is needed to enhance the Raman signals.[13] As such, commercial-available $Au@SiO_2$ nanoparticles, with an Au core (50 ± 10 nm in diameter) and a SiO_2 shell (2 ± 1 nm thickness), were uniformly deposited onto the Cu SA/R-GDY surface to enable the SHINERS

(Figures S31–S35). Figure 4a–c displays the potential trajectories of SHINERS for Cu SA/R-GDY during CO_2RR measurements. The primary distinction of the recorded Raman spectra lies in peaks centered at 525 cm^{-1}, which can be assigned to a Cu–OH mode according to the literature.[14] The Cu–OH band over the Cu SA/F-GDY electrode developed quickly at −0.45 V, and then grew in intensity and blueshifted to 532 cm^{-1} as the potential further decreased to −1.3 V. Whereas, Cu SA/H-GDY displayed a much weaker Cu–OH band until the applied potential was beyond −0.85 V. For Cu SA/OMe-GDY, no obvious Cu–OH band was observed in the applied potential window. It's worth noting that the relative ratio of the pH-dependent HCO_3^-/CO_3^{2-} equilibrium (HCO_3^- at 1015 cm^{-1} and CO_3^{2-} at 1065 cm^{-2}) in the Raman spectra provides a quantitative descriptor to monitor the surface pH.[15] From the recorded Raman spectra, the HCO_3^- band for Cu SA/F-GDY is pronounced over the applied potential range, while that can only be detected at a low potential range from −0.3 V to −0.5 V for Cu SA/H-GDY, and becomes almost invisible for Cu SA/OMe-GDY. We thus inferred that the local pH over the Cu SA/F-GDY surface is lower than that of Cu SA/H-GDY and Cu SA/OMe-GDY electrodes. At −1.3 V, Cu SA/F-GDY exhibits a surface pH of 9.53, obviously below the pH of the bulk solution. Theoretical calculations further verified that Cu SA/F-GDY engendered the lowest pK_a among Cu SA/R-GDY when water coordinates with these Cu catalysts (Figure S36; the pK_a values of adsorbed water are 5.63, 8.47 and 8.24 for Cu SA/F-GDY, Cu SA/H-GDY and Cu SA/OMe-GDY, respectively). Such low local pH is speculated to benefit the CH_4 production pathway.

We further investigate the chemical state of Cu SA/F-GDY and Cu SA/OMe-GDY during CO_2RR by recording in situ EELS via in situ TEM technique (Figure S37). Before exerting potentials, the EELS of Cu L_3-edge of the pristine Cu SA/F-GDY exhibited a higher near-edge position (≈932.8 eV) than that of Cu SA/OMe-GDY (≈931.7 eV), suggesting a higher oxidation state of Cu SA/F-GDY (Figure 4d and Figure S38), which echoes with the XPS and XAFS results. When proceeding with CO_2RR, the corresponding Cu L_3-edge of both samples shifted negatively by varying the potential stepwise from −0.6 V to −1.0 V, demonstrating a reduced Cu valence state at the catalytic centers. By comparing the Cu L_3-edge EELS spectra collected at −1.0 V, we found that the near-edge position of Cu SA/F-GDY (≈931.9 eV) was still higher than that of Cu SA/OMe-GDY (≈931.2 eV), implying that the introduced functional groups are capable to fine-tuning the electronic density of Cu centers even under catalytic conditions. The results also reveal that a positive charge state of Cu centers

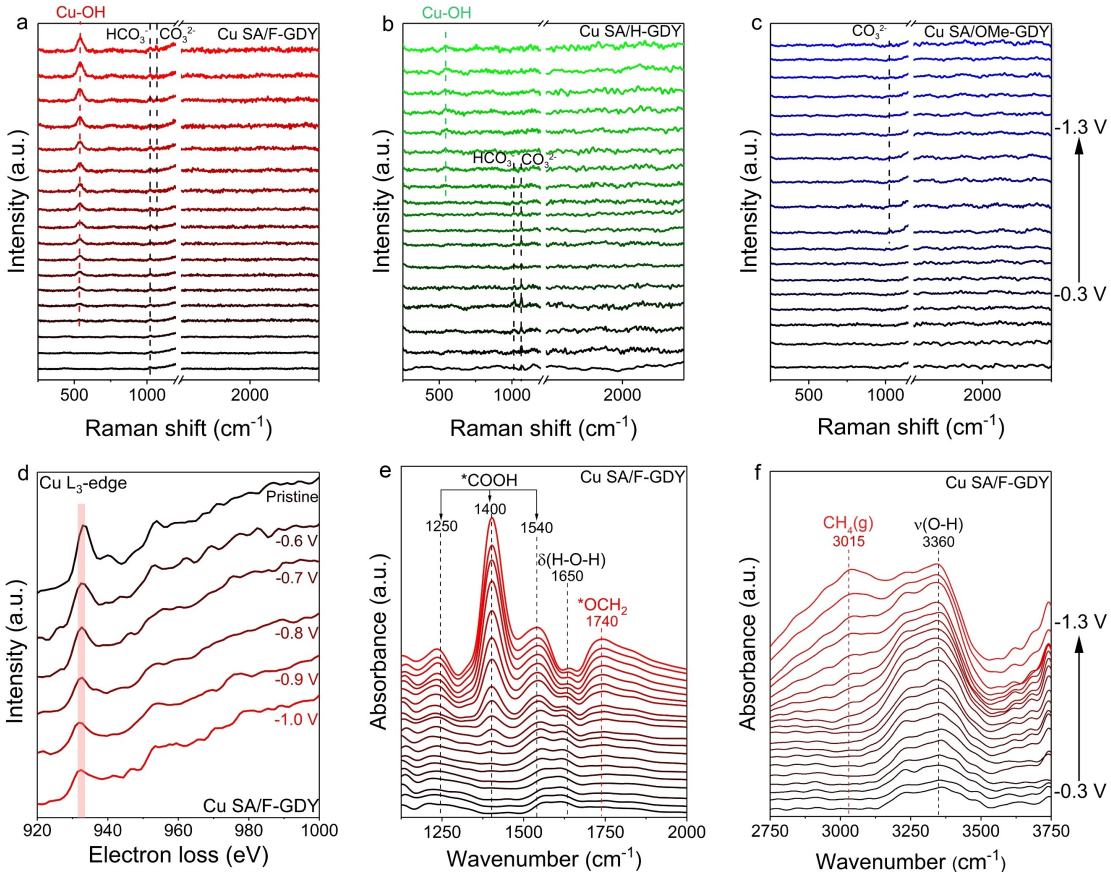

Figure 4. In situ electrochemical spectroscopy and EELS measurements. In situ SHINER spectra of a) Cu SA/F-GDY, b) Cu SA/H-GDY and c) Cu SA/OMe-GDY with Au@SiO_2 in CO_2 at a potential range of −0.3 V to −1.3 V. d) In situ EELS spectra of Cu SA/F-GDY. e), f) In situ ATR-FTIR spectra of Cu SA/F-GDY record at a potential range from −0.3 V to −1.3 V.

over Cu SA/F-GDY is secured, which is an important promotor for CO_2RR activity. The EELS of O *K*-edge and F *K*-edge recorded over Cu SA/OMe-GDY and Cu SA/F-GDY, respectively, present nearly analogous profiles at different applied potentials, signifying that the introduced functional groups were undisturbed under electrolysis (Figure S39). Moreover, we also scrutinize the time-dependent morphology and selected area electron diffraction (SAED) of Cu SA/F-GDY at −1.0 V. As shown in Figures S40 and S41, no apparent changes of morphology and SAED of Cu SA/F-GDY occurred during CO_2RR.

Analysis of the above XAFS, XPS, in situ Raman and in situ EELS results highlighted that the electron-withdrawing group of –F leads to more positive $Cu^{\delta+}$ charge states and promotes the hydrolysis of bound H_2O through the inductive effect. *Consequently, the pK_a of the adsorbed H_2O is decreased, resulting in a more acidic local environment that favors the protonation of CO_2 reduction intermediates for CH_4 production.* In contrast, Cu SA/H-GDY and Cu SA/OMe-GDY with relatively low Cu valance engender high pK_a values of adsorbed H_2O, which is deleterious to the CH_4 selectivity.

To track the surface-bound species and CO_2RR intermediates, in situ ATR-FTIR measurements were conducted. Note that the ATR-FTIR was operated at a CO_2-purged H-cell due to the technical limitation of the ATR-FTIR setup. The electrolyte pH in the H-cell is estimated at 6.98, lower than the pH value in the flow cell reactor. Nevertheless, the distribution of the CO_2 reduction products over Cu SA/R-GDY follows a similar selectivity trend to that under the flow cell tests, except for the higher H_2 efficiency and lower current density (Figure S42). Still, the FE_{CH_4} is proportional to the electron-withdrawing capacity of functional groups around the Cu centers. Cu SA/F-GDY exhibits a high FE_{CH_4} of 53.1 % at −1.3 V, which is 2- and 4-fold higher than those of Cu SA/H-GDY and Cu SA/OMe-GDY, respectively (Figure S43). Figures 4e, f and S44 display the corresponding ATR-FTIR spectra of Cu SA/F-GDY and Cu SA/OMe-GDY at a potential range from −0.3 V to −1.3 V. Four peaks appeared at 1250, 1334, 1400 and 1560 cm^{-1} were attributable to the OH deformation, C–O stretch, symmetric stretch and asymmetric stretch of *COOH, respectively, which is generally regarded as a crucial intermediate for CO/CH_4 formations.[16] Remarkably, an infrared band at ≈1740 cm^{-1} was exclusively revealed on Cu SA/F-GDY, which could be assigned to the surface-bound $*OCH_2$ species,[17] a key intermediate that was speculated for the prevalent CH_4 or CH_3OH formation.[18] The intensity of $*OCH_2$ bands increased as the potential decreased, coinciding with the CH_4 production trends over Cu SA/F-GDY. Furthermore, the band of CH_4 was observed at 3015 cm^{-1} only for Cu SA/F-GDY, suggesting its favorable CH_4 electroproduction (Figure 4f).[19]

To support experimentally observed Cu–OH mode in in situ Raman spectra, we employed the finite difference method to simulate the Raman spectra of *OH on Cu SA/F-GDY at the density functional theory (DFT) level.[20] The calculated Raman spectra show a Cu–OH stretch mode at 575 cm^{-1} (Figure S50a). As one nearby H_2O forms a hydrogen bond with OH*, the same Raman mode undergoes a 10 cm^{-1} redshift (Figure S50b), suggesting the not fully accounted environmental factor could cause the gap between experimentally observed and DFT calculated Cu–OH mode. We further calculate the adsorption-free energies of the reaction intermediates to verify the proposed mechanisms. Based on in situ vibrational spectroscopy, substantial Cu–OH and $Cu–OCH_2$ species have been formed in Cu SA/F-GDY during CO_2RR. Since one CuC_4 site could not hold both OH and CO_2-related species simultaneously without breaking the original $Cu–C_4$ coordination (Figure S45), we conjectured that the reaction might need the cooperation of two adjacent CuC_4 sites (Figure 5b and Figure S46). Therefore, we have proposed an electrocatalytic cycle involving a total of 8 protons/electrons for $CO_2 \rightarrow CH_4$ conversion occurring on two adjacent CuC_4 sites of a double-layer Cu SA/F-GDY model (Figure 5e). Initially, CO_2 is adsorbed to one Cu site close to the H_2O-coordinate Cu site (Figure 5d). Owing to spatial confinement, $*CO_2$ and $*H_2O$ are close enough to form one hydrogen bond to stabilize the bent $*CO_2$. The estimated stabilization energy by the hydrogen bonding is given in Table S3. Then $*CO_2$ is reduced into *COOH by taking a proton from $*H_2O$ and an electron from the electrode, which is stabilized by the *OH on the other Cu-site via hydrogen bonding (Figure S47a). The free energy change of this step is estimated by subtracting the energy of an electron (−4.6 eV) relative to a standard hydrogen electrode at zero potential[21] from the difference of free energies for $*CO_2 + *H_2O + e^- \rightarrow *COOH + *OH$. It can be seen from Figure 5c that the change of free energy from $* + H_2O + CO_2$ to $*COOH + *OH$ is almost the same for all three different catalysts. Then *COOH undergoes a proton-coupled electron transfer (PCET) reaction and generates *CO (Figure S47b). The calculated binding energy of CO (E*CO) on Cu SA/R-GDY (R = –F, –H, –OMe) are −0.948 eV, −1.512 eV and −1.552 eV, respectively (Figure S49). Such sizable binding energies suggest CO will stay on Cu and the desorption of CO will be thermodynamically unfavorable. With the help of *OH, *CO goes through five consecutive PCET reactions and produces *CHO, $*OCH_2$, $*OCH_3$, $*OHCH_3$ and CH_4 successively. Noteworthily, $*OCH_2$ has turned around so that the atom bonding with Cu has switched from C to O (Figures S45c and S45d). After CH_4 is released from the catalyst, both *OH species are reduced into H_2O and released.

The free energy profile of the above-mentioned reaction pathways was calculated at the Perdew–Burke–Ernzerhofer (PBE) level in the presence of a negative charge and implicit solvent effect. As Figure 5a shows, the most likely potential limiting step is the formation of *CHO from *CO, which requires a thermodynamic energy input of 0.82 eV. The next uphill step is $*OCH_2 \rightarrow *OCH_3$. Further, as the –F groups in Cu SA/F-GDY are replaced with –H or –OMe, the formation of *CHO becomes appreciably more endothermic (Cu SA/H-GDY: 1.17 eV, Cu SA/OMe-GDY: 1.06 eV), indicating that Cu SA/F-GDY is more favorable to the production of *CHO (Figure 5c). Besides, the competitive hydrogen reduction reaction may influence the FE_{CH4} of Cu

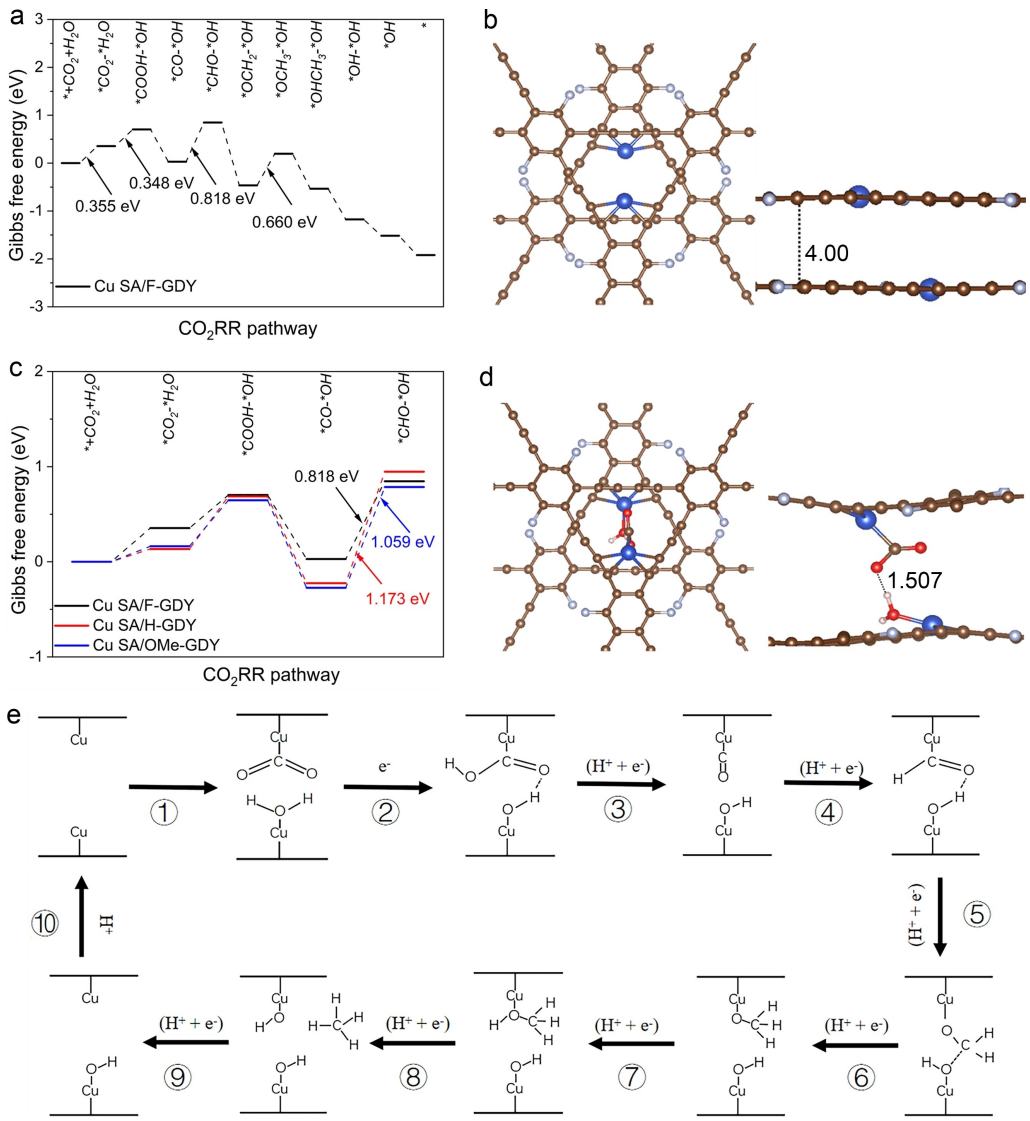

Figure 5. DFT calculation. a) The free-energy diagrams of CO_2 reduction to CH_4 on Cu SA/F-GDY. b) Optimized Cu SA/F-GDY structure, the blue, brown and silver-gray balls represent Cu, C and F atoms. c) Main free-energy profiles from $*CO_2+*H_2O$ to *CHO - *OH for Cu SA/F-GDY (black line), Cu SA/H-GDY (red line) and Cu SA/OMe-GDY (blue line). d) Top and side view of $*CO_2+*H_2O$ (the blue, red, pale pink, brown and silver-gray ball represent Cu, O, H, C and F atoms). e) Proposed CH_4 formation pathway.

SA/OMe-GDY. Hence, we calculate the density of states of adsorbed H of Cu SA/OMe-GDY by DFT. As Figure S51 shows, there is an appreciable overlap between the density of states of *H and Cu atoms below the Fermi level, which indicates strong bonding interaction between them that leads to favorable adsorption of H.

Conclusion

We have constructed a series of Cu SACs on GDY derivatives modified with electron-withdrawing/-donating groups with a view to fine-tuning the charge state of Cu, which is vital to regulating the selectivity and reactivity of CO_2RR. Physical characterizations revealed that the surrounding electron-withdrawing (–F) or -donating (–OMe) groups showed an intriguing electronic push-pull effect on the atomic Cu–C_4 moieties, resulting in the $Cu^{\delta+}$ valence state in order of Cu SA/F-GDY > Cu SA/H-GDY > Cu SA/OMe-GDY. The CO_2RR experiments confirmed that the FE_{CH_4} was proportional to the electron-withdrawing ability of functional groups near Cu centers. In situ spectroscopy of Raman, EELS and ATR-FTIR analysis revealed that the origin of the high CH_4 selectivity over Cu SA/F-GDY is related to the low pK_a of adsorbed H_2O on the positive $Cu^{\delta+}$ surface, which engenders the low local pH and promotes the protonation of CO_2 reduction intermediates toward CH_4 formation. As a result, Cu SA/F-GDY achieves a fairly high FE_{CH_4} of 72.3 % with a j_{CH4} of 174.24 mA cm^{-2} at −1.2 V. A CO_2-to-CH_4 conversion mechanism involving two Cu sites was proposed based on DFT calculations and the common Cu–OH species might be non-innocent for CO_2RR. The

present work opens up the possibility of perturbating the electronic structure of SACs in a molecular way. More broadly, our findings will offer a stepping stone for unraveling the correlations between the electronic structure of SACs and their catalytic properties in many other reactions.

Acknowledgements

This work is supported by the National Natural Science Foundation of China (22179057, 21790351, 22273093, U22A20439), Stable Support Plan Program of Shenzhen Natural Science Fund (20200925152742003), Educational Commission of Guangdong Province (2020KTSCX121) and the CAS Project for Young Scientists in Basic Research (YSBR-005). We thank the staff at the 4B9A beamline of Beijing Synchrotron Radiation Facility(BSRF) for assistance with the XAFS measurement. G.Z.Z. is grateful for the start-up funding of University of Science and Technology of China. The Supercomputing Center of University of Science and Technology of China and Hefei Advanced Computing Center are acknowledged for the computing resource.

Conflict of Interest

The authors declare no conflict of interest.

Data Availability Statement

The data that support the findings of this study are available in the Supporting Information of this article.

Keywords: CO_2 Reduction Reaction · Copper · Electrochemistry · Electronic Perturbation · Single-Atom Catalysts

[1] a) R. M. Bullock, J. G. Chen, L. Gagliardi, P. J. Chirik, O. K. Farha, C. H. Hendon, C. W. Jones, J. A. Keith, J. Klosin, S. D. Minteer, R. H. Morris, A. T. Radosevich, T. B. Rauchfuss, N. A. Strotman, A. Vojvodic, T. R. Ward, J. Y. Yang, Y. Surendranath, *Science* **2020**, *369*, eabc3183; b) C. T. Campbell, *Nat. Chem.* **2012**, *4*, 597–598.

[2] a) Y. Zhou, F. Che, M. Liu, C. Zou, Z. Liang, P. De Luna, H. Yuan, J. Li, Z. Wang, H. Xie, H. Li, P. Chen, E. Bladt, R. Quintero-Bermudez, T.-K. Sham, S. Bals, J. Hofkens, D. Sinton, G. Chen, E. H. Sargent, *Nat. Chem.* **2018**, *10*, 974–980; b) H. Xiao, W. A. Goddard, T. Cheng, Y. Liu, *Proc. Natl. Acad. Sci. USA* **2017**, *114*, 6685–6688; c) S. Nitopi, E. Bertheussen, S. B. Scott, X. Liu, A. K. Engstfeld, S. Horch, B. Seger, I. E. L. Stephens, K. Chan, C. Hahn, J. K. Norskov, T. F. Jaramillo, I. Chorkendorff, *Chem. Rev.* **2019**, *119*, 7610–7672; d) Z. Gu, H. Shen, Z. Chen, Y. Yang, C. Yang, Y. Ji, Y. Wang, C. Zhu, J. Liu, J. Li, *Joule* **2021**, *5*, 429–440.

[3] a) Y. Wang, Z. Chen, P. Han, Y. Du, Z. Gu, X. Xu, G. Zheng, *ACS Catal.* **2018**, *8*, 7113–7119; b) A. Zhang, R. He, H. Li, Y. Chen, T. Kong, K. Li, H. Ju, J. Zhu, W. Zhu, J. Zeng, *Angew. Chem. Int. Ed.* **2018**, *57*, 10954–10958; *Angew. Chem.* **2018**, *130*, 11120–11124; c) X. Yuan, L. Zhang, L. Li, H. Dong, S. Chen, W. Zhu, C. Hu, W. Deng, Z.-J. Zhao, J. Gong, *J. Am. Chem. Soc.* **2019**, *141*, 4791–4794; d) S. He, F. Ni, Y. Ji, L. Wang, Y. Wen, H. Bai, G. Liu, Y. Zhang, Y. Li, B. Zhang, H. Peng, *Angew. Chem. Int. Ed.* **2018**, *57*, 16114–16119; *Angew. Chem.* **2018**, *130*, 16346–16351.

[4] A. Wagner, C. D. Sahm, E. Reisner, *Nat. Catal.* **2020**, *3*, 775–786.

[5] a) X. Cui, W. Li, P. Ryabchuk, K. Junge, M. Beller, *Nat. Catal.* **2018**, *1*, 385–397; b) Y. Chen, R. Gao, S. Ji, H. Li, K. Tang, P. Jiang, H. Hu, Z. Zhang, H. Hao, Q. Qu, *Angew. Chem. Int. Ed.* **2021**, *60*, 3212–3221; *Angew. Chem.* **2021**, *133*, 3249–3258.

[6] a) E. Jung, H. Shin, B.-H. Lee, V. Efremov, S. Lee, H. S. Lee, J. Kim, W. H. Antink, S. Park, K.-S. Lee, *Nat. Mater.* **2020**, *19*, 436–442; b) Y. Mun, S. Lee, K. Kim, S. Kim, S. Lee, J. W. Han, J. Lee, *J. Am. Chem. Soc.* **2019**, *141*, 6254–6262; c) L. Zhang, Y. Jia, G. Gao, X. Yan, N. Chen, J. Chen, M. T. Soo, B. Wood, D. Yang, A. Du, *Chem* **2018**, *4*, 285–297.

[7] a) G. Li, Y. Li, H. Liu, Y. Guo, Y. Li, D. Zhu, *Chem. Commun.* **2010**, *46*, 3256–3258; b) Y. Xue, B. Huang, Y. Yi, Y. Guo, Z. Zuo, Y. Li, Z. Jia, H. Liu, Y. Li, *Nat. Commun.* **2018**, *9*, 1460; c) X. P. Yin, H. J. Wang, S. F. Tang, X. L. Lu, M. Shu, R. Si, T. B. Lu, *Angew. Chem. Int. Ed.* **2018**, *57*, 9382–9386; *Angew. Chem.* **2018**, *130*, 9526–9530; d) W. Rong, H. Zou, W. Zang, S. Xi, S. Wei, B. Long, J. Hu, Y. Ji, L. Duan, *Angew. Chem. Int. Ed.* **2021**, *60*, 466–472; *Angew. Chem.* **2021**, *133*, 470–476.

[8] a) C. Xie, X. Hu, Z. Guan, X. Li, F. Zhao, Y. Song, Y. Li, X. Li, N. Wang, C. Huang, *Angew. Chem. Int. Ed.* **2020**, *132*, 13644–13648; b) J. He, N. Wang, Z. Yang, X. Shen, K. Wang, C. Huang, Y. Yi, Z. Tu, Y. Li, *Energy Environ. Sci.* **2018**, *11*, 2893–2903; c) C. Xing, Y. Xue, B. Huang, H. Yu, L. Hui, Y. Fang, Y. Liu, Y. Zhao, Z. Li, Y. Li, *Angew. Chem. Int. Ed.* **2019**, *58*, 13897–13903; *Angew. Chem.* **2019**, *131*, 14035–14041.

[9] S. Y. Lee, H. Jung, N.-K. Kim, H.-S. Oh, B. K. Min, Y. J. Hwang, *J. Am. Chem. Soc.* **2018**, *140*, 8681–8689.

[10] a) Z. Qu, Y. Li, S. Huang, P. Chen, X. Ma, *Sci. China Chem.* **2017**, *60*, 912–919; b) A. Dandekar, M. A. Vannice, *J. Catal.* **1998**, *178*, 621–639; c) K. I. Hadjiivanov, G. N. Vayssilov, *Adv. Catal.* **2002**, *47*, 307–511.

[11] Q. S. Bhatia, D. H. Pan, J. T. Koberstein, *Macromolecules* **1988**, *21*, 2166–2175.

[12] a) Y.-R. Wang, H.-M. Ding, X.-Y. Ma, M. Liu, Y.-L. Yang, Y. Chen, S.-L. Li, Y.-Q. Lan, *Angew. Chem. Int. Ed.* **2022**, *61*, e202114648; *Angew. Chem.* **2022**, *134*, e202114648; b) L. Zhang, X.-X. Li, Z.-L. Lang, Y. Liu, J. Liu, L. Yuan, W.-Y. Lu, Y.-S. Xia, L.-Z. Dong, D.-Q. Yuan, Y.-Q. Lan, *J. Am. Chem. Soc.* **2021**, *143*, 3808–3816; c) Y. Zhang, L.-Z. Dong, S. Li, X. Huang, J.-N. Chang, J.-H. Wang, J. Zhou, S.-L. Li, Y.-Q. Lan, *Nat. Commun.* **2021**, *12*, 6390; d) J.-D. Yi, R. Xie, Z.-L. Xie, G.-L. Chai, T.-F. Liu, R.-P. Chen, Y.-B. Huang, R. Cao, *Angew. Chem. Int. Ed.* **2020**, *59*, 23641–23648; *Angew. Chem.* **2020**, *132*, 23849–23856; e) S. Chen, B. Wang, J. Zhu, L. Wang, H. Ou, Z. Zhang, X. Liang, L. Zheng, L. Zhou, Y.-Q. Su, D. Wang, Y. Li, *Nano Lett.* **2021**, *21*, 7325–7331; f) S. Chen, Y. Su, P. Deng, R. Qi, J. Zhu, J. Chen, Z. Wang, L. Zhou, X. Guo, B. Y. Xia, *ACS Catal.* **2020**, *10*, 4640–4646; g) Q. Hu, Z. Han, X. Wang, G. Li, Z. Wang, X. Huang, H. Yang, X. Ren, Q. Zhang, J. Liu, C. He, *Angew. Chem. Int. Ed.* **2020**, *59*, 19054–19059; *Angew. Chem.* **2020**, *132*, 19216–19221; h) M. K. Kim, H. J. Kim, H. Lim, Y. Kwon, H. M. Jeong, *Electrochim. Acta* **2019**, *306*, 28–34; i) X. Wang, A. Xu, F. Li, S.-F. Hung, D.-H. Nam, C. M. Gabardo, Z. Wang, Y. Xu, A. Ozden, A. S. Rasouli, A. H. Ip, D. Sinton, E. H. Sargent, *J. Am. Chem. Soc.* **2020**, *142*, 3525–3531; j) L. Han, S. Song, M. Liu, S. Yao, Z. Liang, H. Cheng, Z. Ren, W. Liu, R. Lin, G. Qi, X. Liu, Q. Wu, J. Luo, H. L. Xin, *J. Am. Chem. Soc.* **2020**, *142*, 12563–12567; k) T. Zhang, S. Verma, S. Kim, T. T. Fister, P. J. A.

Kenis, A. A. Gewirth, *J. Electroanal. Chem.* **2020**, *875*, 113862; l) Y. Li, F. Cui, M. B. Ross, D. Kim, Y. Sun, P. Yang, *Nano Lett.* **2017**, *17*, 1312–1317; m) Z. Wang, Q. Yuan, J. Shan, Z. Jiang, P. Xu, Y. Hu, J. Zhou, L. Wu, Z. Niu, J. Sun, T. Cheng, W. A. Goddard, *J. Phys. Chem. Lett.* **2020**, *11*, 7261–7266; n) Y. Cai, J. Fu, Y. Zhou, Y.-C. Chang, Q. Min, J.-J. Zhu, Y. Lin, W. Zhu, *Nat. Commun.* **2021**, *12*, 586.

[13] N. Bodappa, M. Su, Y. Zhao, J.-B. Le, W.-M. Yang, P. Radjenovic, J.-C. Dong, J. Cheng, Z.-Q. Tian, J.-F. Li, *J. Am. Chem. Soc.* **2019**, *141*, 12192–12196.

[14] a) Y. Zhao, X. Chang, A. S. Malkani, X. Yang, L. Thompson, F. Jiao, B. Xu, *J. Am. Chem. Soc.* **2020**, *142*, 9735–9743; b) G. Niaura, *Electrochim. Acta* **2000**, *45*, 3507–3519.

[15] a) X. Lu, C. Zhu, Z. Wu, J. Xuan, J. S. Francisco, H. Wang, *J. Am. Chem. Soc.* **2020**, *142*, 15438–15444; b) N. Heidary, K. H. Ly, N. Kornienko, *Nano Lett.* **2019**, *19*, 4817–4826; c) X. Chen, J. Chen, N. M. Alghoraibi, D. A. Henckel, R. Zhang, U. O. Nwabara, K. E. Madsen, P. J. A. Kenis, S. C. Zimmerman, A. A. Gewirth, *Nat. Catal.* **2021**, *4*, 20–27.

[16] a) S. Zhu, T. Li, W.-B. Cai, M. Shao, *ACS Energy Lett.* **2019**, *4*, 682–689; b) S. Zhu, B. Jiang, W.-B. Cai, M. Shao, *J. Am. Chem. Soc.* **2017**, *139*, 15664–15667.

[17] G. Busca, J. Lamotte, J. C. Lavalley, V. Lorenzelli, *J. Am. Chem. Soc.* **1987**, *109*, 5197–5202.

[18] a) K. J. P. Schouten, Y. Kwon, C. J. M. van der Ham, Z. Qin, M. T. M. Koper, *Chem. Sci.* **2011**, *2*, 1902–1909; b) Y. Hori, R. Takahashi, Y. Yoshinami, A. Murata, *J. Phys. Chem. B* **1997**, *101*, 7075–7081.

[19] a) L. Luo, J. Luo, H. Li, F. Ren, Y. Zhang, A. Liu, W.-X. Li, J. Zeng, *Nat. Commun.* **2021**, *12*, 1218; b) X. Li, Y. Sun, J. Xu, Y. Shao, J. Wu, X. Xu, Y. Pan, H. Ju, J. Zhu, Y. Xie, *Nat. Energy* **2019**, *4*, 690–699.

[20] a) H. Shang, C. Carbogno, P. Rinke, M. Scheffler, *Comput. Phys. Commun.* **2017**, *215*, 26–46; b) H. Shang, N. Raimbault, P. Rinke, M. Scheffler, M. Rossi, C. Carbogno, *New J. Phys.* **2018**, *20*, 073040.

[21] S. Trasatti, *Electrochim. Acta* **1991**, *36*, 1659–1667.

Manuscript received: November 22, 2022
Accepted manuscript online: December 7, 2022
Version of record online: December 28, 2022